Batteries & Supercaps

Research Article
doi.org/10.1002/batt.202500337

Chemistry
Europe
European Chemical
Societies Publishing

www.batteries-supercaps.org

Interface Engineering in Sulfide-Based All-Solid-State Batteries: Insights from Resistance Analysis

Shunsuke Kawaguchi,* Naomi Fukiya, Kei Ehara, Tomoyuki Ichikawa, Manami Yoshimura, Eishi Iso, Yuji Sasaki, Yuhei Horisawa, Masaki Shimada, Minoru Kuzuhara, and Takuhiro Miyuki

All-solid-state batteries (ASSBs) are secondary batteries that utilize solid electrolytes (SEs) as lithium conduction carriers. Consequently, they can potentially replace conventional lithium-ion batteries. To enhance the battery performance, the properties of solid–solid interfaces must be fully understood. However, design guidelines for the formation of solid–solid SE interfaces within electrodes are yet to be formulated. Herein, a resistance analysis is applied to investigate the factors affecting the performance of sulfide-based SEs with different particle sizes in ASSB electrodes. Conventional alternating current impedance spectroscopy and direct current internal resistance measurements reveal a correlation between the SE particle size and the resistance of the cathode electrode. The optimal SE particle size for the positive electrodes in ASSBs is found to vary with the state of charge (SOC) of the battery. Furthermore, the performance of the positive electrode cell is rate-limited when the SOC is below 20%. The findings can be used to formulate effective design guidelines for SEs employed in ASSB electrodes.

1. Introduction

All-solid-state batteries (ASSBs) are next-generation batteries designed to replace lithium-ion batteries (LIBs). ASSBs can be characterized by high energy densities, excellent charge–discharge characteristics, wide operating temperature ranges, and high safety. Their high safety is attributed to the use of solid electrolytes (SEs) instead of flammable liquid electrolytes. As LIBs are required to operate at increasingly higher energy densities,[1] the higher safety of ASSBs becomes a key feature for their wider adoption.

The electrochemical performance of ASSBs is limited by the low ionic conductivity of the electrolyte[2] and the high resistance at the solid–solid interface.[3] In particular, the formation and long-term stability of the solid–solid interface are key design aspects that must be extensively investigated.[4] To this end, SE selection is crucial, and numerous types of electrode materials based on sulfides,[5] oxides,[6] chloride,[7] polymers,[8] and hydrides[9] have been studied. Sulfide-based SEs can overcome some of the aforementioned challenges because they exhibit both high ionic conductivity and high formability. Different sulfide-based SEs, including argyrodite-type $Li_{7-x}PS_{6-x}Cl_x$ (LPSCl),[10,11] LGPS-type $Li_{10+x}Ge_{1+x}P_{2-x}S_{12}$ (LGPS),[12,13] and glass-ceramic-type $Li_2S–P_2S_5–LiI$ (LPSI), have been evaluated.[14,15] Recently, SEs with ion conductivities comparable to those of liquid electrolytes[16] and SEs with extremely high formability[17] have also been developed.

Despite these advancements, other challenges continue to hinder the utilization of SEs as electrode layers. For example, ASSBs with sulfide-based SE electrodes encounter a trade-off between the battery performance and the applied pressure required to form the electrode.[18] This suggests that the solid–solid interface within the electrode is not adequately formed at low applied pressures. Moreover, the SE particle size affects its interaction with the active material (AM) within the electrode, which in turn is strongly correlated with the battery performance.[19,20] This is because smaller SE particles create more contact points with the AM, forming more conductive pathways within the electrode. In addition to the SE particle size, the particle size distribution is another important factor.[21] In summary, in addition to determining the ionic conductivity and formability of the electrode, the morphology of SEs in ASSB electrodes, specifically the particle size and distribution, strongly affects the electrode performance. Hence, design guidelines for the effective formation of solid–solid interfaces must be proposed via a thorough examination of how these factors influence the battery performance.

In this study, we investigated the impact of the SE particle size on the formation of solid–solid interfaces in ASSB electrode layers through a resistance analysis, with the goal of establishing suitable design guidelines for the formation of such interfaces. We employed the generalized galvanostatic intermittent titration technique (GITT), which is a common analytical method, to evaluate the cell resistance under different state of charge (SOC) values.[22] Moreover, to identify the different cell resistances, we applied

S. Kawaguchi,[+] N. Fukiya, K. Ehara, T. Ichikawa, M. Yoshimura, E. Iso, Y. Sasaki, Y. Horisawa, M. Shimada, M. Kuzuhara, T. Miyuki
Consortium of Lithium Ion Battery Technology and Evaluation Research Center (LIBTEC)
1-8-31 Midorigaoka, Ikeda, Osaka 563-8577, Japan
E-mail: kawaguchi.shunsuke@libtec.or.jp, shunsuke-kawaguchi@mail.nissan.co.jp
[+]Present address: Nissan Motor Co., Ltd., 1, Natsushima-cho, Yokosukashi, Kanagawa 237-8523, Japan

Batteries & Supercaps

Research Article
doi.org/10.1002/batt.202500337

Chemistry
Europe
European Chemical
Societies Publishing

alternating current impedance spectroscopy using symmetric cells.[23] By combining direct current (DC) and alternating current (AC) methods, we found that the optimal SE particle size in the cathode layer varies depending on the SOC region. This phenomenon has not been reported for liquid-based LIBs and is unique to ASSBs.[24] Our study demonstrates that the impact of SE particle size on the performance of the ASSB electrode layer can be quantified using a simple analysis method. Our findings contribute to the creation of design guidelines for the formation of solid–solid interfaces in ASSBs.

2. Results and Discussion

To investigate the impact of SE particle size on the electrode layer in ASSBs, two types of SEs with different particle sizes were examined. Table S1, Supporting Information presents the electrode performance of the two types of cathode layers prepared using large-particle-size $Li_{7-x}PS_{6-x}Cl_x$ (LPSCl) (D50: ca. 6 µm) (L_SE) and small-particle-size LPSCl (D50: ca. <1 µm) (S_SE). The ionic and electronic conductivities were measured using previously described methods.[25,26] Our results revealed that L_SE exhibited higher ionic conductivity values, attributed to the significant dependence of the ionic conductivity of the cathode layer on the ionic conductivity of the SE.[26] However, no significant difference was observed in the electronic conductivities of the different electrodes. This is because the electronic conductivity of the cathode layer depends on the electronic conductivity of the AM.[27,28]

Figure 1 compares the discharge rates of the cathode half-cells prepared using S_SE and L_SE. The discharge curves corresponding to 0.1C nearly coincide, with differences observed only in the low-SOC region. To ensure optimal cathode performance, the forming pressure and the stack pressure during cell assembly were set to 600 and 200 MPa, respectively, based on previous studies (see Section 4).[29] L_SE tended to have a lower discharge capacity than S_SE, consistent with previously observed trends studies.[30–32] However, the overvoltage load

Figure 1. Discharge rate test results for cathode half-cells prepared using S_SE and L_SE. Charging is performed at 0.1C (CC.CV mode) and discharging at 0.1C, 0.5C, 1C, and 2C (CC mode). The figure shows excerpts of the discharge curves at 0.1C and 2C.

in the discharge curve exhibited a trend reversal during discharge. In other words, up to a certain point in the discharge process, the overvoltage was lower for L_SE. This suggests that the influence of the ionic conductivity dominated the discharge process up to this point. The discharge behavior at 2C became more pronounced, with the discharge curves crossing each other. Therefore, the discharge behavior between S_SE and L_SE differed depending on the SOC.

Figure 2 shows the EIS measurement results of the cathode half-cells. At SOC 50%, L_SE has a lower resistance (Figure 2a). At SOC 0%, S_SE has a lower total resistance (Figure 2b). This is consistent with the electrode characteristics inferred from the discharge curves shown in Figure 1. Generally, LIBs based on liquid electrolytes do not exhibit such a behavior even if the electrolyte is changed. This is a unique characteristic specific to ASSBs.[33] In both the EIS measurements, the resistance of the In-Li electrode affected the results, making precise classification of the resistance components difficult.[34,35]

Therefore, the resistance originating from the cathode was determined by fabricating a symmetric cell and performing EIS measurements. **Figure 3**a,b shows the EIS measurement results of the cathode symmetric cell at 50 and 0% SOC, respectively. No change in the resistance sequence can be observed at either SOC. As expected, the resistance of the cathode layer varied with the SE particle size, and the resistance components differed depending on the SOC. Although this dependence on the SOC has not been widely discussed in previous studies,[36,37] it is considered an important factor in practical cells. As a control, a half-cell was reassembled using the cathode retrieved from the disassembled symmetric cell, and no significant change in the electrochemical performance was observed (Figure S3, Supporting Information).

Resistance measurements and classification were performed based on the GITT test results to analyze the differences in the resistance and SOC dependence observed in the symmetric cell. The resistance measurements were conducted at SOC intervals of 1% based on the capacity conversion (Figure S4 and S5, Supporting Information), and the resistances were separated by isolating the resistance values observed in the symmetric cell based on the time constants of each resistance (Figure S6, Supporting Information). **Figure 4** shows the discharge curves obtained from the GITT tests. In normal charge and discharge cycles, both S_SE and L_SE showed similar behaviors, whereas in the GITT tests, differences in their behavior became visible. As shown in the figure, the discharge behavior in the GITT test can be divided into three regions. In Region I, L_SE exhibits a smaller IR drop and overall overvoltage than S_SE. This behavior is characteristic of liquid-phase LIBs and is attributed to the difference in the ionic conductivity of the electrolyte.[38,39] In Region II, a similar behavior is observed; however, initially, it is difficult to see a clear difference between S_SE and L_SE. This is attributed to the reduction in the resistance of the cathode layer with decreasing SOC, which minimizes the difference.[36,37] The differences in the values of the different resistance components will be discussed later. In Region III, both S_SE and L_SE exhibit a cutoff voltage at which the discharge is terminated. This is due to an
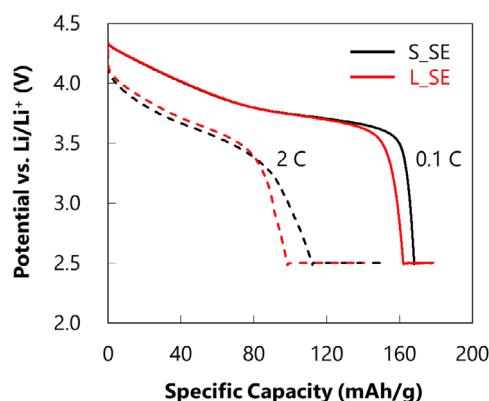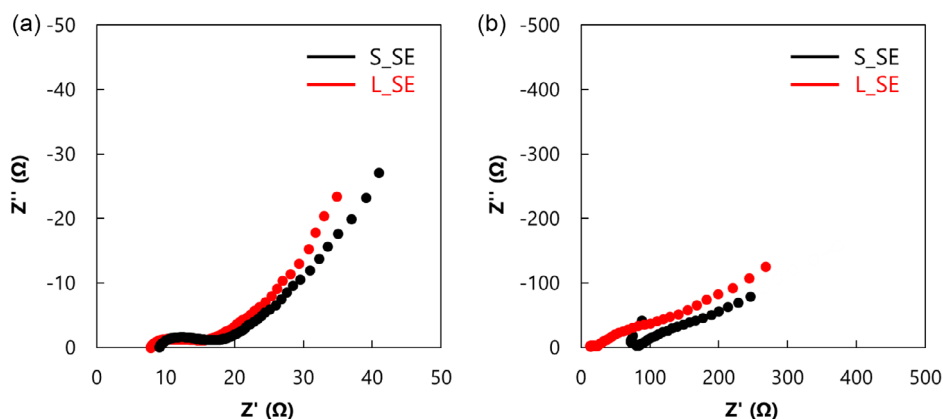
Batteries & Supercaps

Research Article
doi.org/10.1002/batt.202500337

Chemistry Europe
European Chemical
Societies Publishing

Figure 2. Electrochemical impedance spectroscopy (EIS) measurement results of the cathode half-cell at a) SOC 50% and b) SOC 0%. After reaching each potential, EIS measurements are performed following a 4-h open-circuit voltage (OCV) relaxation.
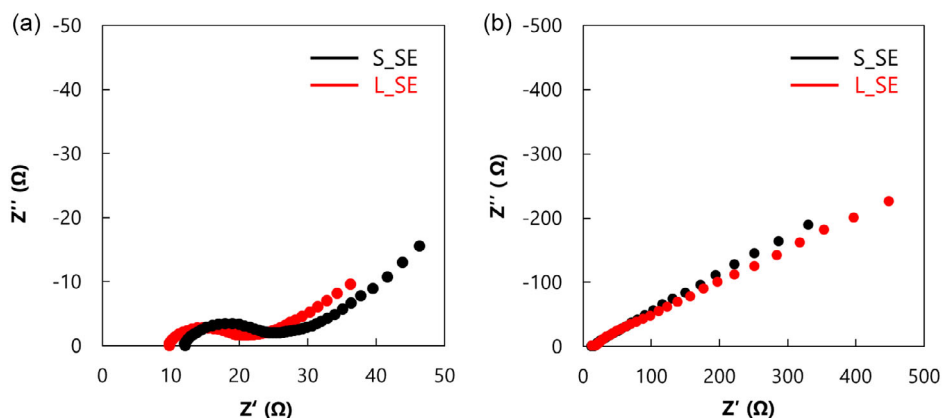

Figure 3. EIS measurement results of the cathode symmetric cell at a) SOC 50% and b) SOC 0%. After reaching each potential, the cell is allowed to relax for 4 h under OCV and then disassembled to create a symmetric cell. Finally, EIS measurements are conducted.
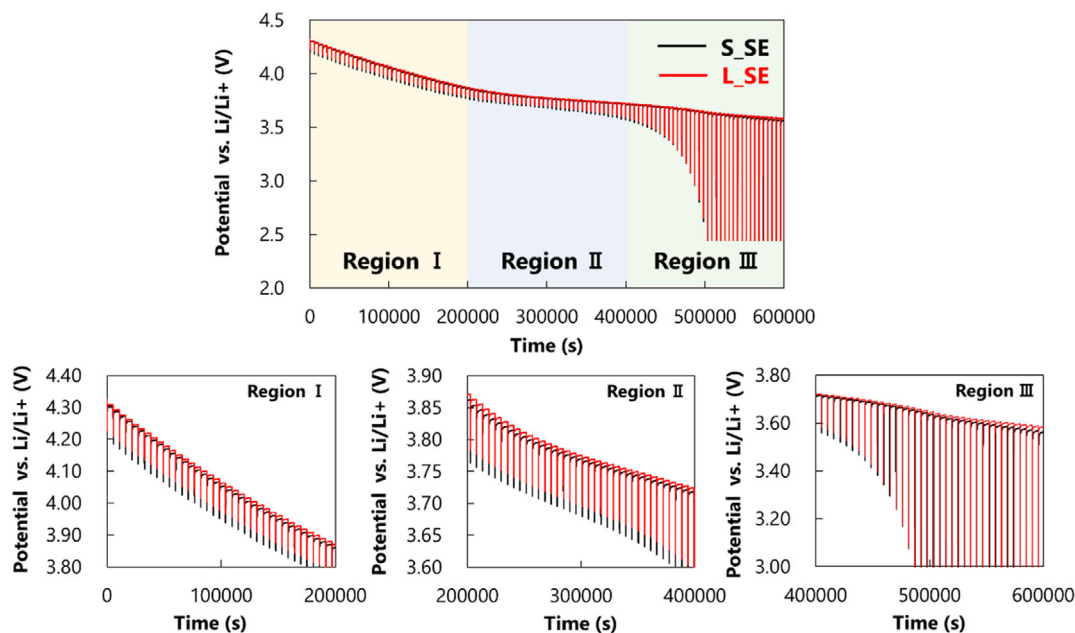

Figure 4. Results of discharge galvanostatic intermittent titration technique (GITT) tests for cathode half-cells prepared using S_SE and L_SE. Each discharge step corresponds to 1% SOC in terms of capacity. The measurement time is divided into three regions: Regions I, II, and III.

© 2025 Wiley-VCH GmbH

Batteries & Supercaps

Research Article
doi.org/10.1002/batt.202500337

Chemistry Europe
European Chemical
Societies Publishing

increase in the resistance of the cathode layer at low SOC.[38,39] L_SE exhibits a lower potential drop at each discharge step, and the discharge progresses more gradually. Therefore, in the low-SOC region, the S_SE cathode layer has a lower resistance. In summary, the differences in SE particle sizes within the cathode layer have a significant impact on the resistance components within the cathode. Not only can changes in the typical charge–discharge curves be observed, but further information can be obtained through more detailed analysis. Previous studies have also shown that differences in SE particle size affect battery performance,[30–32] and this type of resistance analysis may provide useful information for developing design guidelines.

Figure 5a shows the total resistance values of the prepared cell at each SOC measured using GITT. In terms of the potential, the resistance of the cathode layer is lowest at ≈3.8 V. This corresponds to an SOC of ≈50%, which is in good agreement with previous results.[38,39] Therefore, the resistance values at each SOC in the GITT test accurately reflect the behavior of the cathode layer. Furthermore, the resistance values obtained from the GITT were roughly consistent with the resistance values measured from the symmetric cell EIS at SOC 0 and 50% (Figure S7, Supporting Information). Based on this, the resistance values from the GITT test can be divided into three regions using the time constants of each resistance from the symmetric cell EIS. Consequently, the resistances that occurred during charge and discharge can be analyzed in detail (Figure S5, Supporting Information). The main advantage of linking the

results of the GITT test with the EIS results is that it allows the resistance components for each SOC to be separated. It is thus possible to more thoroughly analyze the unique phenomenon observed in Figure 1. The three resistances are classified as follows. $R1$ represents the contact resistance and the resistance due to the cell itself. $R1$ can be used to determine the electronic conductivity of the electrode. $R2$ represents the charge transfer resistance (R_{ct}) that occurs between the AM and SE. Finally, $R3$ represents the resistance arising from the diffusion of Li ions in the AM (Figure S6, Supporting Information). Figure 5b–d shows the SOC dependence of the resistance values in each region, classified based on the GITT and symmetric cell EIS measurements. In Figure 5b, no significant difference in the $R1$ values or SOC dependence is observed between S_SE and L_SE. The resistance values in this region correspond to very high-frequency ranges when converted to time constants; therefore, they are strongly influenced by the measurement accuracy of the equipment used.[40] In Figure 5c, L_SE exhibits a lower resistance than S_SE for SOC values above 20%. This result is consistent with previously discussed test results and suggests that the difference in ionic conductivity plays a role. However, for SOC values below 20%, the resistance of the cathode layer increases significantly, and L_SE becomes more resistive than S_SE. In other words, in the region with the highest resistance of the cathode layer, S_SE is the superior cathode material. This trend can be visualized from the discharge curves shown in Figure 2. Figure 5d shows a trend similar to that shown in Figure 5c;
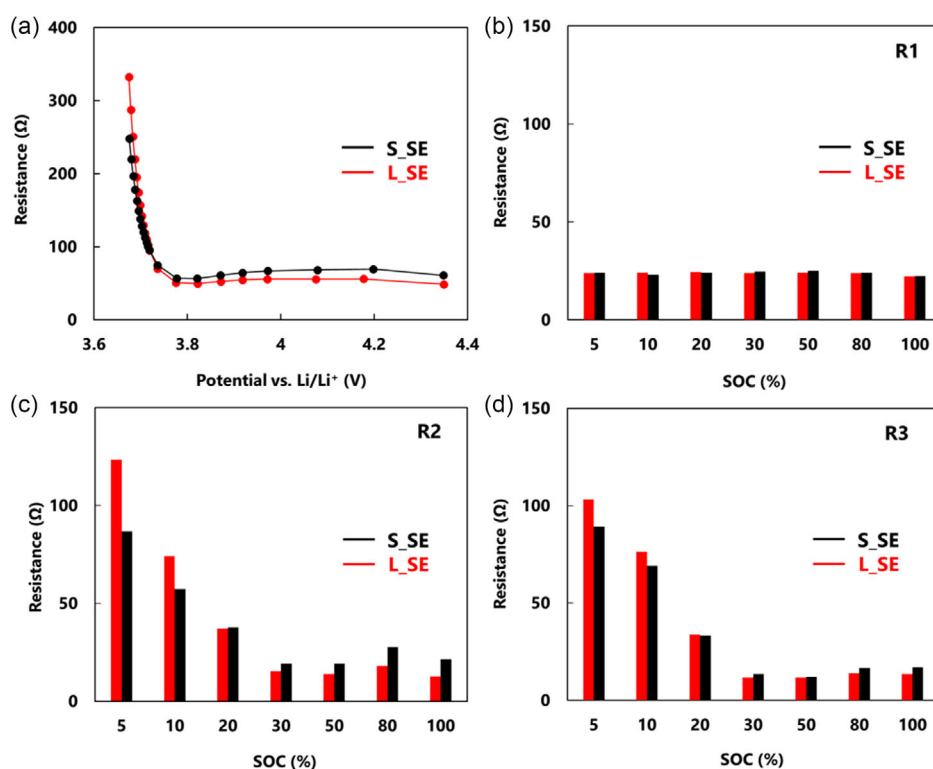

Figure 5. a) Total resistance values of the cell under each SOC measured in the GITT test. b–d) Classification results of the resistances measured in the GITT test. The resistance components are classified based on the time constants of each resistance component obtained from the symmetric cell. (b) $R1$: contact resistance, (c) $R2$: charge transfer resistance, and (d) $R3$: diffusion resistance.

however, the difference in the resistance between S_SE and L_SE is more pronounced in this region. Therefore, the resistance values in Figure 5d strongly influence the performance-limiting behavior of the cathode layer. Previous studies have reported the importance of Li conduction through diffusion in ASSBs,[41] and our results correlate well with these findings. From the above results and the resistance analysis, the performance levels of S_SE and L_SE are reversed at an SOC of ≈20%.

Figure 6a–d compares the electrochemical performance of S_SE and L_SE from practical charge and discharge rate tests. Figure 6a,b shows the results of the charge rate tests for S_SE and L_SE, respectively. Both the capacity values and retention ratios clearly indicate that L_SE exhibits superior charge rate performance to S_SE (Figure S8, Supporting Information). This finding supports the conclusion that, except in the extremely low SOC region, ionic conductivity plays a dominant role in determining the cathode performance. In contrast, Figure 6c,d shows the discharge rate performance, where S_SE outperforms L_SE, exhibiting a trend opposite to that observed during charging (Figure S8, Supporting Information). As discussed for the contents of Figure 5, this contrasting behavior can be attributed to the different contributions of the cathode resistance components depending on the SOC. Even at a low rate of 0.1C, L_SE delivers a lower discharge capacity than S_SE, suggesting that the AM becomes isolated in L_SE at low SOC.[30–32]

Previous studies have reported that contact loss between the AM and SE can occur during charge–discharge cycling. In fact, our observations revealed that the electrochemical contact states of S_SE and L_SE reverse as a function of the SOC during cycling (Figure S9, Supporting Information).[42] While L_SE exhibits higher ionic conductivity, its larger particle size may hinder the maintenance of intimate contact with the AM due to structural rearrangements within the cathode caused by volumetric changes during cycling. Although a detailed analysis of this contact degradation is required, the critical insight here is that both S_SE and L_SE exhibited a performance trade-off depending on the SOC region.

To realize cathodes with excellent electrochemical characteristics across the entire SOC range, this trade-off must be resolved by simultaneously optimizing ionic conductivity and interfacial contact between the AM and SE.[43,44] A possible strategy is the hybridization of large- and small-particle SEs; however, a selective placement of the particles within the cathode microstructure poses a significant challenge.[45] As mentioned earlier, the SOC-dependent relationship between the SE particle size and battery performance is unique to ASSBs and warrants further investigation. For example, future work should consider tuning particle size distributions or absolute particle size and evaluating correlations with the mechanical properties of the cathode. Most importantly, the methodology presented herein offers a viable approach to optimize the SE particle size within the cathode structure. This framework can be applied to develop rational design guidelines for the electrode architecture in ASSBs, ultimately accelerating their practical implementation and widespread adoption.
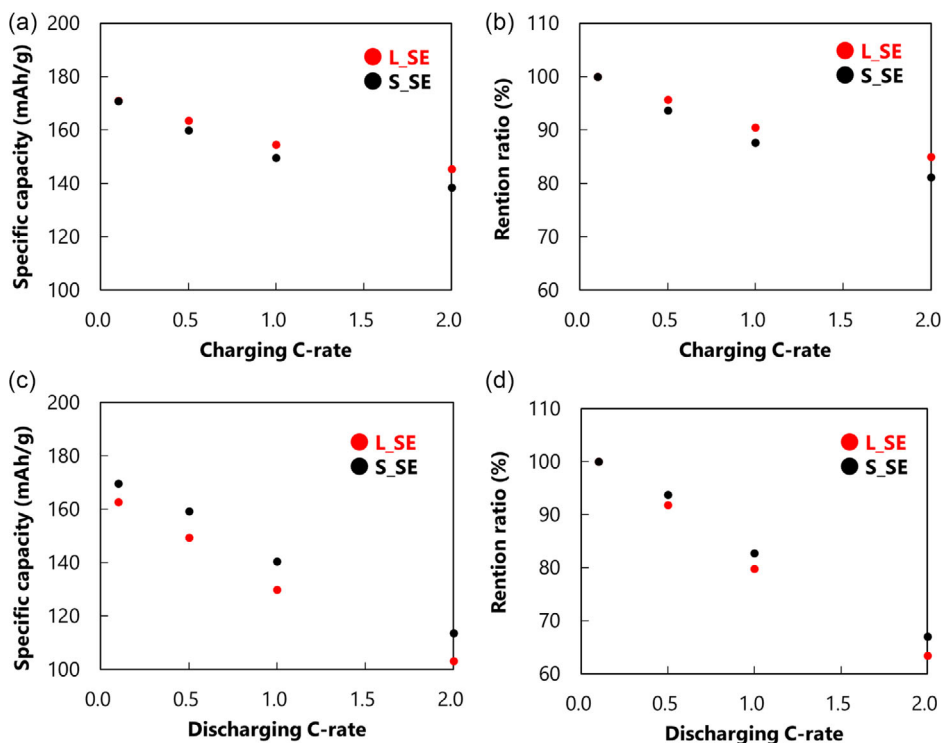

Figure 6. a,b) Charging test results for cathode half-cells prepared using S_SE and L_SE. c,d) Discharging test results for cathode half-cells prepared using S_SE and L_SE.

3. Conclusion

To investigate the impact of the SE particle size on the cathode layer of ASSBs, a resistance analysis was conducted using both DC and AC methods. Cathode layers with large-particle-size SEs exhibited lower resistance values than those with small-particle-size SEs at SOC values above 20% when converted to capacity. This suggests that the ionic conductivity plays a significant role in this SOC region. However, for SOC values below 20%, the resistance of the cathode layer increased significantly, whereas the resistance of the cathode layer with small-particle-size SE decreased. This indicates that in regions with a higher cathode resistance, a uniform contact between the AM and SE, as well as the formation of conductive pathways, are critical. These resistance correlations were in good agreement with the trends observed in the actual charge and discharge rate tests.

Considering the tradeoff between the SE particle size and ionic conductivity, a clear solution for optimizing the SE particle size for each SOC region cannot be provided at this time. Nevertheless, we clearly established that the optimal SE particle size in the cathode layer of ASSBs varies with the SOC—or more precisely, that distinct design parameters may be more effective at different SOC levels. This insight can be useful in the rational design of next-generation ASSB electrodes. Optimization can be implemented using conventional resistance analysis techniques which are simple and practical. The application of resistance analysis to a wide range of materials can help establish effective design guidelines for high-performance ASSB cathodes.

4. Experimental Section

Material Preparation

Cathodes were prepared using $LiNi_{0.5}Co_{0.2}Mn_{0.3}O_2$ (NCM523). The SEs were obtained from Mitsui Mining & Smelting Co., Ltd. and comprised two types of argyrodite-type SEs ($Li_{7-x}PS_{6-x}Cl_x$: LPSCl), with average particle sizes of ca. 6 and ca. <1 μm, respectively. Vapor-grown carbon fiber (Resonac Holdings Corporation) served as the conductive additive.

Electrochemical Measurement of SE Samples

For each SE, 100 mg of the sample was weighed and subjected to a uniaxial mechanical press at a pressure of 100 MPa for 1 min. The SE powder was then pressed at 600 MPa for 1 min in a uniaxial mechanical press machine to form pellets. These pellets were stacked in a SUS foil/SE pellet/SUS foil configuration and sealed, and then fastened by a bolt to reach an applied pressure of 200 MPa. The ionic conductivity was measured using EIS at frequencies of up to 7 MHz, and the resistance was extracted from the Nyquist plot using a VSP-300 multichannel potentiostat (Biologic).

Cathode Half-Cell Preparation (Performance Test)

The cathode layer was prepared by adding the AM, SE, and a conductive additive at a ratio of 75:22:3 (wt%) and mixing them for ca. 15 min in a mortar. First, an SE layer was formed using LPSCl (100 mg) and pressed at 100 MPa for 1 min. The composite material (22 mg) was added to each half-cell, and the working electrode was pressed at 100 MPa for another 1 min to form the cathode and SE stacking layers. The stacked layer was pressed at 900 MPa for 1 min and then combined with the electrode material. The cells were assembled using In-Li as the counter electrode. The current density for each half-cell was set to 1C at 3 mA cm^{-2}.

Cathode Half-Cell Preparation (Symmetric-Cell Test)

A different type of cathode half-cell was fabricated to evaluate the symmetric cell. First, 100 mg of LPSCl was added, and forming was performed at 100 MPa for 1 min. Subsequently, 22 mg of the cathode material was added, and the formation was repeated at 100 MPa for 1 min. Subsequently, the main forming process was performed at 900 MPa for 1 min to firmly bond the cathode and SE layers. After forming, 100 mg of LPSCl was added again, and forming was performed at 100 MPa for 1 min, followed by forming at 900 MPa for 1 min. This process created an interface between the SE layers, enabling the separation of the upper and lower sides of the SE layers when the cell was disassembled (Figure S1, Supporting Information). In addition, no significant performance difference was observed in the cell with the two-layered SE structure (Figure S2, Supporting Information).

Cathode Half-Cell Test

The fabricated cathode half-cell was allowed to stand for 8 h in the OCV state to stabilize the potential. Thereafter, it was connected to a VSP-300 multichannel potentiostat and subjected to three cycles of charging and discharging at 0.1C/0.1C (CC.CV mode) in the voltage range of 3.0–4.35 V versus Li/Li+. After these cycles, the cell was charged again at 0.1C to an SOC of 50% based on capacity and then allowed to relax for 4 h. Once the potential was stabilized, EIS measurements were performed at frequencies ranging from 10 mHz to 1 MHz using an alternating current amplitude of 10 mV. After the cathode half-cell test, GITT tests were performed on the cells that showed no abnormalities.

GITT Test

A GITT test was conducted on the cathode half-cell to evaluate the dependence of the cathode cell resistance on the SOC. First, charging was performed at 0.1C (CC.CV mode) and then discharging at 0.5C for 72 s, followed by a relaxation period of 5000 s. After the relaxation was completed, a second discharge at 0.5C for 72 s was performed, followed by another 5000 s of relaxation. One discharge cycle corresponds to a 1% change in the SOC of the cell in terms of capacity (Figure S3, Supporting Information). The test was concluded when potential fluctuations ceased after repeated discharges.

Symmetric Cell Test

The fabricated cathode half-cell was allowed to stand for 8 h at the OCV state to stabilize the potential. Subsequently, three final charging and discharging cycles were applied in the same manner. After the test, the fabricated cathode half-cell was left in the OCV state for 8 h to stabilize its potential. The cell was then transferred to a glove box in an argon atmosphere (dew point: ca. −80 °C; oxygen concentration: <1 ppm), where the stack was disassembled. As mentioned earlier, the SE layer, which was formed into two layers, was

Batteries & Supercaps

Research Article
doi.org/10.1002/batt.202500337

Chemistry Europe
European Chemical
Societies Publishing

decomposed, starting from the SE layer; thus, a symmetric cell was created by stacking the cathode and SE layers together. In the fabrication of the symmetric cells, cathodes equilibrated to the same SOC were paired to represent a desired charge state. The symmetric cell was subjected to EIS measurements at frequencies ranging from 10 mHz to 1 MHz with an alternating current amplitude of 10 mV.

Glossary

ASSB	All-solid-state battery
LIB	Lithium ion battery
NCM	$LiNi_xCo_yMn_{1-x-y}O_2$
SE	Solid electrolyte
LPSBH	$Li_3PS_4 \cdot xLiBH_4$
LPSCl	$Li_{7-x}PS_{6-x}Cl_x$
LGPS	$Li_{10+x}Ge_{1+x}P_{2-x}S_{12}$
LPSI	$Li_2S–P_2S_5–LiI$
EIS	Electrochemical impedance spectroscopy
CC	Constant current
CV	Constant voltage

Conflict of Interest

The authors declare no conflict of interest.

Author Contributions

Shunsuke Kawaguchi: conceptualization, research planning, experimentation, curation, and writing and editing of the paper. **Naomi Fukiya**: experimentation, curation. **Kei Ehara**: experimentation, curation. **Tomoyuki Ichikawa**: experimentation, curation. **Manami Yoshimura**: experimentation, curation. **Eishi Iso**: experimentation, curation. **Yuji Sasaki**: experimentation, curation. **Yuhei Horisawa**: experimentation, curation. **Masaki Shimada**: conceptualization, research planning, experimentation, curation. **Minoru Kuzuhara**: supervision of research. **Takuhiro Miyuki**: supervision of research. All authors discussed, revised, and finally approved the manuscript.

Data Availability Statement

The data that support the findings of this study are available from the corresponding author upon reasonable request.

[1] T. Wulandari, D. Fawcett, S. B. Majumder, G. E. J. Poinern, *Battery Energy* **2023**, *2*, 20230030.

[2] S. Randau, D. A. Weber, O. Kötz, R. Koerver, P. Braun, A. Weber, E. Ivers-Tiffée, T. Adermann, J. Kulisch, W. G. Zeier, F. H. Richter, J. Janek, *Nat. Energy* **2020**, *5*, 259.

[3] K. Takada, N. Ohta, L. Zhang, K. Fukuda, I. Sakaguchi, R. Ma, M. Osada, T. Sasaki, *Solid State Ionics* **2008**, *179*, 1333.

[4] L. Xu, S. Tang, Y. Cheng, K. Wang, J. Liang, C. Liu, Y.-C. Cao, F. Wei, L. Mai, *Joule* **2018**, *2*, 1991.

[5] C. J.L.Wang, Y. Zhao, M. Zheng, L. Xi, X. Sun, *Energy Environ. Sci.* **2021**, *14*, 2577.

[6] V. Venkataraman, M. Pérez-Fortes, L. G. Wang, *J. Energy Storage* **2019**, *24*, 100782.

[7] T. Asano, A. Sakai, S. Ouchi, M. Sakaida, A. Miyazaki, S. Hasegawa, *Adv. Mater.* **2018**, *30*, 1803075.

[8] X. Xu, Y. Wang, Q. Yi, X. Wang, R. A. P. Camacho, H. Kungl, R. A. Eichel, L. Lu, H. Zhang, *ChemSusChem* **2023**, *16*, e202202152.

[9] S.-I. Orimo, Y. Nakamori, J. R. Eliseo, A. Züttel, C. M. Jensen, *Chem. Rev.* **2007**, *107*, 4111.

[10] N. Masuda, K. Kobayashi, F. Utsuno, T. Uchikoshi, N. Kuwata, *J. Phys. Chem. C* **2022**, *33*, 14067.

[11] L. Xi, D. Zhang, X. Xu, Y. Wu, F. Li, S. Yao, M. Zhu, J. Liu, *ChemSusChem* **2023**, *16*, e202202158.

[12] N. Kamaya, K. Homma, Y. Yamakawa, M. Hirayama, R. Kanno, M. Yonemura, T. Kamiyama, Y. Kato, S. Hama, K. Kawamoto, A. Mitsui, *Nat. Mater.* **2011**, *10*, 682.

[13] Y. Kato, S. Hori, T. Saito, K. Suzuki, M. Hirayama, A. Mitsui, M. Yonemura, H. Iba, R. Kanno, *Nat. Energy* **2016**, *1*, 16030.

[14] J. Lau, R. H. DeBlock, D. M. Butts, D. S. Ashby, C. S. Choi, B. S. Dunn, *Adv. Energy Mater.* **2018**, *8*, 1800933.

[15] Z. Wu, S. Chen, C. Yu, C. Wei, L. Peng, H.-L. Wang, S. Cheng, J. Xie, *Chem. Eng. J.* **2022**, *442*, 136346.

[16] Y. Li, S. Song, H. Kim, K. Nomoto, H. Kim, X. Sun, S. Hori, K. Suzuki, N. Matsui, M. Hirayama, T. Mizoguchi, T. Saito, T. Kamiyama, R. Kanno, *Science* **2023**, *381*, 50.

[17] A. Sakuda, T. Takeuchi, M. Shikano, H. Sakaebe, H. Kobayashi, *Front. Energy Res.* **2016**, *4*, 19.

[18] H.-J. Shin, J. T. Kim, A.-Y. Kim, N. Noh, J. Park, C. R. Park, S. Yu, H. Kim, K. Y. Chung, J. M. Yuk, S.-T. Myung, H.-G. Jung, *Adv. Energy Mater.* **2023**, *13*, 2301220.

[19] T. Shi, Q. Tu, Y. Tian, Y. Xiao, L. J. Miara, O. Kononova, G. Ceder, *Adv. Energy Mater.* **2019**, *2*, 1902881.

[20] F. Strauss, T. Bartsch, L. de Biasi, A. Y. Kim, J. Janek, P. Hartmann, T. Brezesinski, *ACS Energy Lett.* **2018**, *3*, 992.

[21] C. Yu, S. Ganapathy, H. E.R., H. Wang, S. Basak, Z. Li, M. Wagemaker, *Nat. Commun.* **2017**, *8*, 1086.

[22] A. Nickol, T. Schied, C. Heubner, M. Schneider, A. Michaelis, M. Bobeth, G. Cuniberti, *J. Electrochem. Soc.* **2020**, *167*, 090546.

[23] C. H. Chen, J. Liu, K. Amine, *J. Power Sources* **2001**, *96*, 321.

[24] K. M. Shaju, G. V. S. Rao, B. V. R. Chowdari, *Electrochim. Acta* **2003**, *48*, 2691.

[25] Z. Shiroma, *J. Power Sources* **2016**, *316*, 215.

[26] N. Kaiser, S. Spannenberger, M. Schmitt, M. Cronau, Y. Kato, B. Roling, *J. Power Sources* **2018**, *396*, 175.

[27] R. Amin, Y.-M. Chiang, *J. Electrochem. Soc.* **2016**, *163*, 1512.

[28] S.-D. Lee, K.-N. Jung, H. Kim, H.-S. Shin, S.-W. Song, M.-S. Park, J.-W. Lee, *ChemSusChem* **2017**, *10*, 2175.

[29] S. Kawaguchi, N. Fukiya, K. Ehara, T. Ichikawa, M. Yoshimura, E. Iso, Y. Sasaki, Y. Horisawa, Y. Mizukoshi, M. Shimada, N. Ishida, M. Kuzuhara, K. Kawamoto, T. Miyuki, *Adv. Mater.* **2025**, e07963, https://doi.org/10.1002/adma.202507963.

[30] T. Shi, Q. Tu, Y. Tian, Y. Xiao, L. J. Miara, O. Kononova, G. Ceder, *Adv. Energy Mater.* **2020**, *10*, 1902881.

[31] E. Schlautmann, A. Weiß, O. Maus, L. Ketter, M. Rana, S. Puls, V. Nickel, C. Gabbey, C. Hartnig, A. Bielefeld, W. G. Zeier, *Adv. Energy Mater.* **2023**, *13*, 2302309.

[32] K. Otani, T. Muta, T. Furuta, T. Miyuki, T. Kaburagi, G. Inoue, *J. Energy Storage* **2023**, *58*, 106279.

[33] J. Liu, H. Chen, J. Xie, Z. Sun, N. Wu, B. Wu, *J. Power Sources* **2014**, *251*, 208.

[34] N. Togasaki, A. Nakao, T. Tanaka, U. Harada, H. Onishi, H. Yasuda, S. Kobayashi, F. Maeda, T. Osaka, *J. Electrochem. Soc.* **2023**, *170*, 050519.

[35] S. Hori, R. Kanno, X. Sun, S. Song, M. Hirayama, B. Hauck, M. Dippon, S. Dierickx, E. Ivers-Tiffée, *J. Power Sources* **2023**, *556*, 232450.

[36] S. Yanev, H. Auer, R. Pertsch, C. Heubner, K. Nikolowski, M. Partsch, A. Michaelis, *J. Electrochem. Soc.* **2024**, *171*, 050530.

[37] G. H. Chang, H. U. Choi, S. Kang, J.-Y. Park, H.-T. Lim, *Ionics (Kiel)* **2020**, *26*, 1555.

[38] A. Verma, K. Smith, S. Santhanagopalan, D. Abraham, K. P. Yao, P. P. Mukherjee, *J. Electrochem. Soc.* **2017**, *164*, A3380.

[39] T. Schied, A. Nickol, C. Heubner, M. Schneider, A. Michaelis, M. Bobeth, G. Cuniberti, *ChemPhysChem* **2021**, *22*, 885.

[40] Z. Chang, G. A. M. Pop, G. C. M. Meijer, *Biomed. Eng. IEEE Trans.* **2008**, *55*, 1247.

[41] S. Hafner, H. Guthrey, S. Lee, C. Ban, *J. Power Sources* **2019**, *431*, 17.

[42] S. Kawaguchi, H. Yasuda, W. Ogihara, H. Sano, M. Kuzuhara, T. Miyuki, *J. Colloid Interface Sci.* **2025**, *696*, 137878.

[43] Y. Seino, T. Ota, K. Takada, A. Hayashi, M. Tatsumisago, *Energy Environ. Sci.* **2014**, *7*, 627.

[44] A. I. Gebi, O. Dolokto, L. Mereacre, U. Geckle, H. Radinger, M. Knapp, H. Ehrenberg, *ChemSusChem* **2024**, *17*, e202300809.

[45] M. So, G. Inoue, K. Park, K. Nunoshita, S. Ishikawa, Y. Tsuge, *J. Power Sources* **2022**, *530*, 231279.